Magnetar oscillations - I. Strongly coupled dynamics of the crust and the core

Hoven, M. van; Levin, Y.

Magnetar oscillations – I. Strongly coupled dynamics of the crust and the core

Maarten van Hoven[1]★ and Yuri Levin[1,2]★

[1]*Leiden Observatory and Lorentz Institute, Leiden University, PO Box 9513, NL-2300 RA Leiden, the Netherlands*
[2]*School of Physics, Monash University, PO Box 27, VIC 3800, Australia*

ABSTRACT

Quasi-periodic oscillations (QPOs) observed at the tail end of soft gamma repeaters giant flares are commonly interpreted as the torsional oscillations of magnetars. From a theoretical perspective, the oscillatory motion is influenced by the strong interaction between the shear modes of the crust and magnetohydrodynamic Alfvén-like modes in the core. We study the dynamics which arises through this interaction, and present several new results. (1) We show that discrete *edge modes* frequently reside near the edges of the core Alfvén continuum, and explain using simple models why these are generic and long-lived. (2) We compute the magnetar's oscillatory motion for realistic axisymmetric magnetic field configurations and core density profiles, but with a simplified model of the elastic crust. We show that one may generically get multiple gaps in the Alfvén continuum. One obtains strong discrete *gap modes* if the crustal frequencies belong to the gaps; the resulting frequencies do not coincide with, but are in some cases close to the crustal frequencies. (3) We deal with the issue of tangled magnetic fields in the core by developing a phenomenological model to quantify the tangling. We show that field tangling enhances the role of the core discrete Alfvén modes and reduces the role of the core Alfvén continuum in the overall oscillatory dynamics of the magnetar. (4) We demonstrate that the system displays transient QPOs when parts of the spectrum of the core Alfvén modes contain discrete modes which are densely and regularly spaced in frequency. The transient QPOs are the strongest when they are located near the frequencies of the crustal modes. (5) We show that if the neutrons are coupled into the core Alfvén motion, then the post-flare crustal motion is strongly damped and has a very weak amplitude. We thus argue that magnetar QPOs give evidence that the proton and neutron components in the core are dynamically decoupled and that at least one of them is a quantum fluid. (6) We show that it is difficult to identify the high-frequency 625-Hz QPO as being due to the physical oscillatory mode of the magnetar, if the latter's fluid core consists of the standard proton–neutron–electron mixture and is magnetized to the same extent as the crust.

Key words: stars: magnetars – stars: neutron – stars: oscillations.

1 INTRODUCTION

Since the discovery of quasi-periodic oscillations (QPOs) in the light curves of giant flares from soft gamma repeaters (SGR; Barat et al. 1983; Israel et al. 2005; Strohmayer & Watts 2005; Watts & Strohmayer 2006) there has been considerable interest in their physical origin. One of the appealing explanations is that the QPOs are driven by torsional oscillations[1] of the neutron stars whose magnetic energy powers the flares (Duncan 1998). This opens a unique possibility to perform an asteroseismological analysis of neutron stars, and possibly obtain a new observational window to study the neutron star interiors. Many authors have considered torsional modes to be confined to the magnetar crust, and have shown that seismological information about such modes would strongly

---

[1] By torsional oscillations we mean those which are nearly incompressible. Modes with compression have strong restoring forces and feature much higher frequencies than most of the observed QPOs.

★E-mail: vhoven@strw.leidenuniv.nl (MvH); yuri@strw.leidenuniv.nl (YL)

constrain the physics of the crust (Piro 2005; Watts & Strohmayer 2006; Samuelsson & Andersson 2007; Watts & Reddy 2007; Steiner & Watts 2009).

However, it was quickly understood that the theoretical analysis of magnetar oscillations is complicated by the presence of an ultrastrong magnetic field ($B \sim 10^{14}$–10^{15} G) that is frozen into the neutron star and penetrates both the crust and the core. The field provides a channel for an intense hydromagnetic interaction between the motion of the crust and the core, which becomes effective on the time-scale of $\ll 1$ s (Levin 2006, hereafter L06). Since the QPOs are observed for hundreds of seconds after the flare, it is clear that the coupled motion of the crust and the core must be considered. In recent years, significant theoretical effort has gone into the study of this problem (e.g. Glampedakis, Samuelsson & Andersson 2006; Levin 2007, hereafter L07; Gruzinov 2008b; Lee 2008). This paper's analysis is based, in part, on an approach of L07.

To make progress in computing the coupled crust–core motion, L07 has studied the time evolution of an axisymmetric toroidal displacement of a star with axisymmetric poloidal magnetic field. In that case the Alfvén-type motions on different flux surfaces decouple from each other, a well-known fact from previous magnetohydrodynamic (MHD) studies (for a review see Goedbloed & Poedts 2004, hereafter GP). One can then formulate the full dynamics of the system in terms of discrete modes of the crust which are coupled to a continuum of Alfvén modes in the core. L07 demonstrated that (i) the global modes with frequencies inside the continuum are strongly damped via a phenomenon known in MHD as *resonant absorption* (see GP), and (ii) in many cases, asymptotically the system tends to oscillate with the frequencies close to the continuum edges. This result was later confirmed by Gruzinov (2008b), who has used a powerful analytical technique to solve the L07's normal-mode problem (Gruzinov noted that the resonant absorption is mathematically equivalent to Landau damping). Oscillations near the continuum edge frequencies were also observed in a number of numerical general relativistic MHD simulations of purely fluid stars (Sotani, Kokkotas & Stergioulas 2008; Cerda-Duran, Stergioulas & Font 2009; Colaiuda, Beyer & Kokkotas 2009).

Apart from finding QPOs near the continuum edges, L07's dynamical simulations identified transient QPOs with drifting frequencies; these were transiently amplified near the crustal frequencies. No explanation for the origin of the drifts was given.

In this paper, we extend the previous analyses of the hydromagnetic crust–core coupling in an essential way. In Section 2, we re-analyse L07's toy model of a single oscillator coupled to a continuum, and we show that this system generically contains the *edge normal modes* with frequencies near the continuum edges. We show that these modes dominate the late-time dynamics of the system, and develop a formalism which allows one to predict analytically the edge-mode's amplitude from the initial data. We then explore the effect of viscosity on the system (introduced as a friction between the neighbouring continuum oscillators), and show that the edge mode is longer lived than all other motions of the system. We also provide a non-trivial analytical formula for the time dependence of the overall energy dissipation.

In Section 3, we describe how transient QPOs, not associated with the normal modes of the system, are obtained when parts of the core spectrum consist of densely and regularly spaced discrete modes (and in Section 5 we show that such an array of discrete modes is expected when the magnetic field in the core is not perfectly axisymmetric but has some degree of tangling). As a by-product of our analysis, we explain the origin of the QPO frequency drifts seen in L07 simulations. We provide simple analytical fits to the drifts,

and show that when the regularity of the continuum sampling is removed (e.g. when the frequencies are sampled as random numbers picked from the continuum range), the drifts disappear.

In Section 4, we set up models with a more realistic hydromagnetic structure of the neutron star core. We show how to find the continuum modes and their coupling to the crust for an arbitrary axisymmetric poloidal field, with an arbitrary density profile on the core (L07s calculations, for simplicity and concreteness, were restricted to constant density core and homogeneous magnetic field). We treat a more complicated case of a mixed axisymmetric toroidal–poloidal field, with radial stratification, in the Appendix B. We demonstrate that for realistic field configurations, the Alfvén continuum of modes coupled to the crust may show a number of gaps. If a crustal-mode frequency belongs to one of these gaps, a strong global discrete mode arises which dominates the late-time dynamics and whose frequency also belongs to the gap. The frequency of the gap global mode does not generally coincide with, but is often close to that of the crust. We suggest that it was these gap modes that appeared in Lee's (2008) calculations as well-defined discrete global modes.

So far, only axisymmetric magnetic fields have been considered in the magnetar–QPO literature, with the Alfvén continuum modes occupying the flux surfaces of the field. In Section 5 we argue that if the field is not axisymmetric but instead is highly tangled, then the Alfvén continuum modes become localized within small regions of individual field lines, and therefore become dynamically unimportant. Instead, a set of discrete Alfvén modes appears, with the spacing between the modes strongly dependent on the degree of field tangling. We devise a phenomenological prescription which allows us to parametrize the field tangling for computing the dynamically important modes, and introduce an easily solvable 'square box' model suitable for exploring the parameter range.

Finally, in Section 6, we use the suite of models built in the previous sections to explore their connection to the QPO phenomenology. We find that

(a) within the standard magnetar model, it is possible to produce strong long-lived or transient QPOs with frequencies in the range of around 20–150 Hz, but only if the neutrons are decoupled from the Alfvén-like motion of the core; this implies that at least one of the baryonic components of the core is a quantum fluid;

(b) our models could not produce the high-frequency 625-Hz QPO within the standard paradigm of a magnetar core composition.

2 AN OSCILLATOR COUPLED TO A CONTINUUM: EDGE MODES

In this section, we study the motion of a harmonic oscillator (which we hereafter call the large oscillator) which is coupled to a continuum of modes.[2] This model was introduced in L07 and it provides a qualitative insight into the behaviour of crustal modes (represented by the large oscillator) coupled to a continuum of Alfvén modes in the core of a magnetar. L07 found that if the large oscillator's proper frequency was within the range of the continuum frequencies, then the late-time behaviour of the system was dominated by oscillatory motion near the edges of the continuum interval. Here, we give an explanation of this phenomenon in terms of the *edge modes*. Our

---

[2] In many areas of physics similar models have been studied, notably in quantum optics and plasma physics. By contrast with the case studied here, in these models the range of the continuum frequencies is not limited.
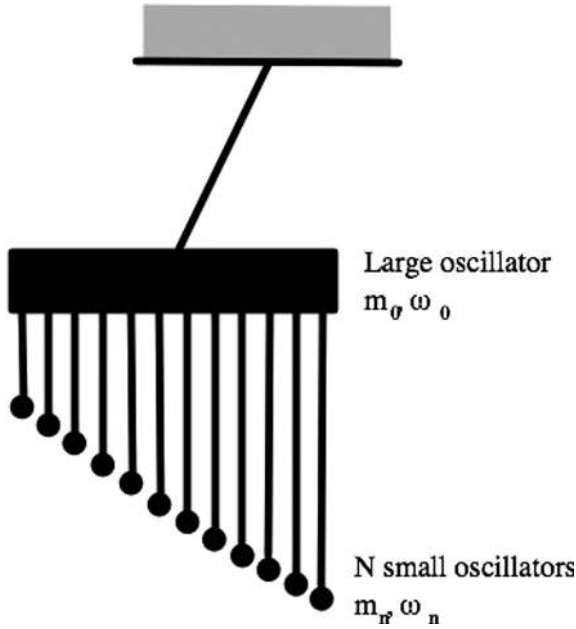
Figure 1. Schematic picture of the toy model. A large number N of small pendulae, representing the (quasi-) continuum, are coupled to one large pendulum, representing the crust.

analysis allows us to use initial data and predict the displacement amplitudes and frequencies of the system at late times.

The model consists of the large mechanical oscillator with mass M and proper frequency ω_0, representing a crustal elastic shear mode. Attached to the large oscillator is a set of N smaller oscillators of mass m_n and proper frequency ω_n constituting a quasi-continuum of frequencies ω_n (where $n = 1, 2, \ldots, N$). The continuum is achieved when $N \to \infty$ while the total small oscillator mass Σm_n remains finite. The convenient pictorial representation is through suspended pendulae, as shown in Fig. 1 (see also fig. 2 of L07).

The equations of motion are obtained as follows. Each small oscillator is driven by the motion of the large oscillator:

$$\ddot{x}_n + \omega_n^2 x_n = -\ddot{x}_0, \tag{1}$$

where x_n is the displacement of the nth small oscillator in the frame of reference of the large oscillator, x_0 is the displacement of the large oscillator in the inertial frame of reference and the right-hand side represents the non-inertial force acting on the small oscillator due
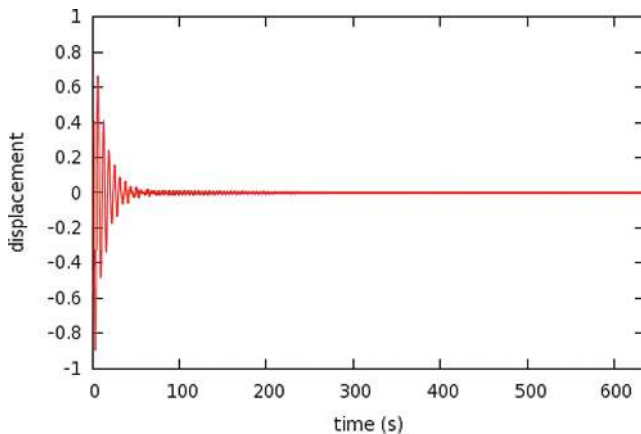
to the acceleration of the large one. The large oscillator experiences the combined pull of the small ones:

$$M\ddot{x}_0 + M\tilde{\omega}_0^2 x_0 = \sum_i m_i \omega_i^2 x_i. \tag{2}$$

Here $\tilde{\omega}_0$ is the frequency of the big pendulum corrected for the mass loading by the small pendulae, i.e. $\tilde{\omega}_0^2 = \omega_0^2 (M + \sum_i m_i)/M$.

2.1 Time-dependent behaviour

In this section we explore the behaviour of this system by direct numerical simulations. We found this to be helpful in the building of our intuition. We defer a semi-analytical normal mode analysis to the next section.

We follow L07 and for concreteness concentrate on a specific example; it will be clear that the conclusions we reach are general. We choose $\omega_0 = 1 \, \text{rad s}^{-1}$ and mass $M = 1$. We choose a total number of 1000 small pendulae with frequencies $\omega_n = (0.5 + n/1000) \, \text{rad s}^{-1}$ and masses $m_n = m = 10^{-4}$, to mimic the continuum frequency range between 0.5 and 1.5 rad s^{-1}. The simulation is initiated by displacing the large oscillator while keeping the small pendulae relaxed (this mimics the stresses in the crust), and then releasing. The subsequent motion of the system is then followed numerically by using a second-order leapfrog integration scheme which conserves the energy with high precision. The resulting motion of the large pendulum can be decomposed into three stages (see Figs 2 and 3).

(1) During the first 50–60 s, there is a rapid exponential decay of the large oscillator's motion, during which most of the energy is transferred to the multitude (i.e. the 'continuum') of small oscillators. This is the so-called phenomenon of 'resonant absorption', which has been studied for decades in the MHD and plasma physics community (e.g. Ionson 1978; Hollweg 1987; GP; L07; Gruzinov 2008b). In this first stage, the amplitude of the big pendulum motions drops by a factor of $\sim$100.

(2) After $\sim$60 s, the exponential decay stops abruptly as the large oscillator now reacts to the collective pull of the small ones. This second stage is characterized by a slow algebraic decay of the amplitude of the big pendulum displacement. Gruzinov (2008b) explains this as being due to the branch cut in the oscillator's response function.
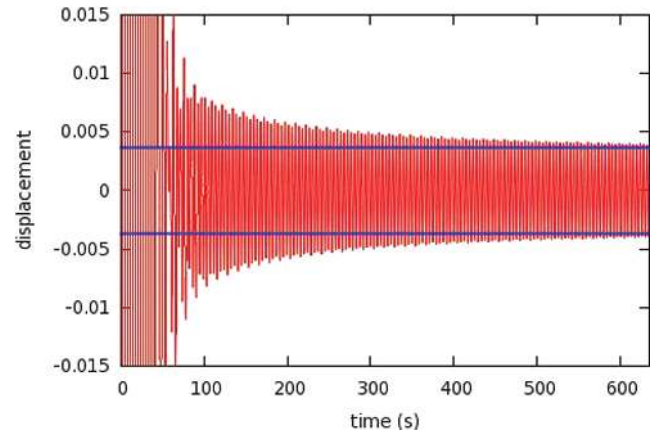

Figure 2. Displacement of the big oscillator as a function of time.

Figure 3. A zoomed-in version of Fig. 2. The blue horizontal lines denote the theoretically predicted amplitude of the dominating upper edge mode (see Section 2.3).
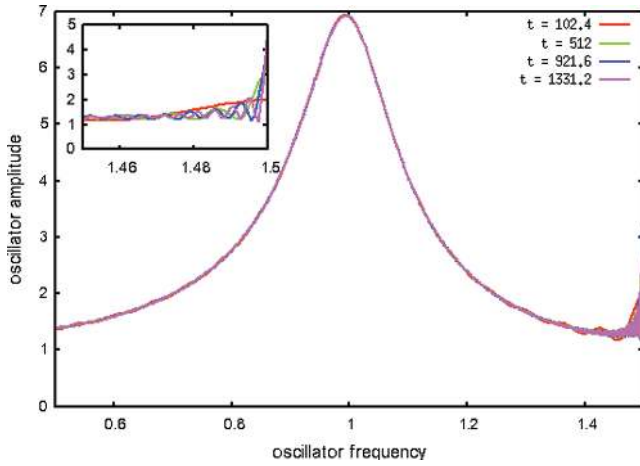
Figure 4. The coloured curves show the amplitudes of the small oscillators during the numerical simulation, at different times t.
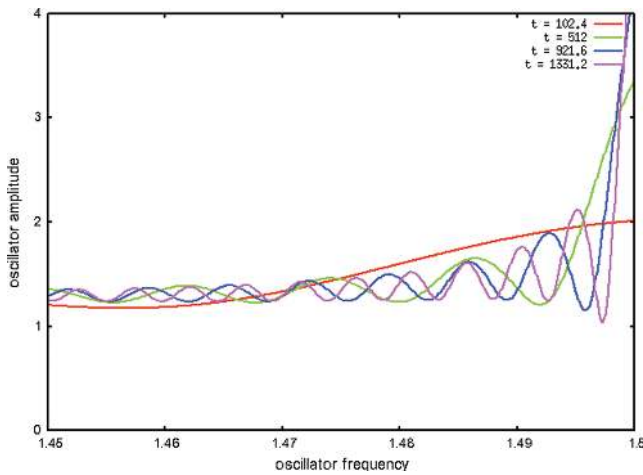

Figure 5. A zoomed-in version of Fig. 4. At later times energy is transferred to the oscillators near the edge of the continuum.

(3) The motion of the large oscillator stabilizes at a constant level (L07 missed this stage in his simulations, which he stopped too early). Fourier transform reveals two QPOs at the frequencies close to the continuum edges, $\omega = 0.5$ and 1.5; the same QPO frequencies can be observed in the previous stage (2) as well.

What is the origin of the QPOs, and how is this eventual stability established? In Figs 4 and 5, we show how the amplitude of the small oscillators evolves with time.

After the initial resonant absorption phase, the amplitude is distributed as a Lorentzian centred on the frequency around $\omega = 1$; this is because the small oscillators in resonance with the large one are the ones which gain the most energy. However, in subsequent times we see that the energy exchange occurs between the small oscillators,[3] and that the net result of this exchange is the energy flow towards the oscillators whose frequencies are near the edges. By the time the third stage begins, the amplitudes of the oscillators near the edge stabilize and their phases become locked. They are pulling and pushing the large oscillator in unison. In the next section, we

---

[3] This is much akin to the well-known phenomenon of resonant energy exchange between two equal-frequency pendulae hanging on the same supporting wall.

show that this behaviour is due to the presence of the *edge normal modes*, and we shall derive their frequencies and amplitudes.

2.2 Finding eigenmodes

In this section we deal with the system of coupled harmonic oscillators, and one should be able to find its normal modes using the standard techniques (Landau & Lifshitz, *Mechanics*, Section 23). However, the fact that all small oscillators are attached to the large one, and there is no direct coupling between the small oscillators, allows us a significant shortcut (in Appendix A, we treat a more general problem of *several* large oscillators coupled to a multitude of the core modes). We proceed as follows.

Suppose that we impose on the large oscillator a periodic motion with angular frequency Ω, by driving it externally with the force $F_{\text{ext}} = F_0(\Omega) \exp(i\Omega t)$. This motion in turn drives the small oscillators according to equation (1):

$$\ddot{x}_n + \omega_n^2 x_n = \Omega^2 x_0, \tag{3}$$

which has the steady state solution:

$$x_n = \frac{\Omega^2}{\omega_n^2 - \Omega^2} x_0, \tag{4}$$

where we have omitted the time-dependent factor $\exp(i\Omega t)$ on both sides. The combined force f_{cont} of the small oscillators acting back on the large one (see equation 2) is given by

$$f_{\text{cont}}(\Omega) = \sum_n m_n \omega_n^2 \frac{\Omega^2}{\omega_n^2 - \Omega^2} x_0. \tag{5}$$

According to Newton's second law,

$$F_0(\Omega) + f_{\text{cont}}(\Omega) = -M\left(\Omega^2 - \omega_0^2\right) x_0. \tag{6}$$

If Ω corresponds to the normal-mode frequency, then $F_0(\Omega) = 0$. Hence by substituting equation (5) into equation (6) we get the following eigenvalue equation for Ω:

$$G(\Omega) = M\left(\omega_0^2 - \Omega^2\right) - \sum_n m_n \omega_n^2 \frac{\Omega^2}{\omega_n^2 - \Omega^2} = 0. \tag{7}$$

In the continuum limit $N \to \infty$, the above equation becomes

$$G(\Omega) = M\left(\omega_0^2 - \Omega^2\right) - \int_{\omega_{\text{min}}}^{\omega_{\text{max}}} d\omega \rho(\omega)\omega^2 \frac{\Omega^2}{\omega^2 - \Omega^2} = 0, \tag{8}$$

where $\rho(\omega) = dm/d\omega$ is the mass per unit frequency of the continuum modes.

In the discrete case, the solutions of equation (7) are $N - 1$ frequencies Ω_i that are within the quasi-continuum ($\omega_i < \Omega_{i+1} < \omega_{i+1}$, for $i = 1, 2, \ldots, N - 1$; 'quasi-continuum modes'), and two modes with frequencies Ω_{low} and Ω_{high} that are near the edges, but outside, of the continuum (we will refer to these modes as 'edge modes' from now on). In other words, Ω_{low} is in general slightly smaller than the lowest frequency in the continuum, i.e. $\Omega_{\text{low}} \lesssim \omega_1$ and Ω_{high} is slightly larger than the highest frequency in the continuum, i.e. $\Omega_{\text{high}} \gtrsim \omega_N$. It can be shown from equation (7) that in the limit $N \gg 1$ and $m_n \ll M$, the contribution of the small oscillator to the ith quasi-continuum mode is completely dominated by the pendulae that are in close resonance with the mode. More precisely, one can show that as the number of oscillators N increases and m_n decreases, the number of small oscillators contributing to the mode energy remains constant. However, for the two edge modes there is no such singular behaviour in the limit of large N, and consequently they play a special role in the dynamics of the system.

This last point is clearly seen in the continuum case represented by equation (8). The eigenvalue equation has no real solutions in the range of small oscillator continuum $\omega_{\min} < \Omega < \omega_{\max}$, since the response function $G(\Omega)$ is ill defined in this interval.[4] However, the edge modes on both sides of the continuum interval remain, and their frequencies can be found by numerically evaluating the zero-points of $G(\Omega)$ in equation (8). For the numerical of the previous section, one finds $\Omega_{\mathrm{low}} = 0.5 - 8.2 \times 10^{-6}$ and $\Omega_{\mathrm{high}} = 1.5 + 8.6 \times 10^{-4}$. Analytically, one can find the following scaling for the distance $\delta\omega_{\mathrm{edge}}$ between the mode frequency and the nearest edge ω_{edge} of the continuum range:

$$\frac{\delta\omega_{\mathrm{edge}}}{\omega_{\mathrm{edge}}} = C \exp\left\{ -\frac{M\left|\Omega_0^2 - \omega_{\mathrm{edge}}^2\right|}{\rho(\omega_{\mathrm{edge}})\omega_{\mathrm{edge}}^3} \right\}, \tag{9}$$

where C is a constant of order unity. The larger is the density of continuum modes at the edge $\rho(\omega_{\mathrm{edge}})$, the further is the edge mode pushed away from the continuum range. It is particularly interesting to consider the case when the continuum interval is limited by a turning point (L07) with the divergent density of states near the edge, $\rho(\omega) = A/\sqrt{|\omega - \omega_{\mathrm{edge}}|}$, where A is a constant. In this case the distance from the edge-mode frequency to the nearest continuum edge is given by

$$\frac{\delta\omega_{\mathrm{edge}}}{\omega_{\mathrm{edge}}} = C \left\{ \frac{A\omega_{\mathrm{edge}}^{7/2}}{M\left|\Omega_0^2 - \omega_{\mathrm{edge}}^2\right|} \right\}^2. \tag{10}$$

The quadratic dependence in equation (10) versus the exponential dependence in equation (9) implies that the continua with turning points typically feature much more pronounced edge modes and stronger QPOs than the ones with linear edges. In the next section, we show how to calculate the edge-mode amplitudes and QPO strengths from the initial data.

2.3 Late-time behaviour of the system

In the continuum limit, the only modes with real oscillatory frequency are the edge modes. Thus, as we demonstrate explicitly below, they dominate the late-time dynamics of the system when the number N of small oscillators becomes large. Our analysis proceeds as follows.

Lets define a new set of variables, expressed as a vector $\boldsymbol{X}$ with components $X_0 = \sqrt{M}x_0$ and $X_n = \sqrt{m_n}(x_0 + x_n)$ for $n = 1, \ldots, N$. With these new variables, the kinetic energy of the system is a trivial quadratic expression:

$$K = \frac{1}{2}\dot{\boldsymbol{X}} \cdot \dot{\boldsymbol{X}}, \tag{11}$$

where the inner product of two vectors $\boldsymbol{A}$ and $\boldsymbol{B}$ is defined as $\boldsymbol{A} \cdot \boldsymbol{B} = \Sigma_{j=0}^{N} A_j B_j$. The potential energy is a positive-definite quadratic form, whose exact form is unimportant here. The mutually orthogonal eigenmodes $\boldsymbol{X}^i$ can be found via a procedure outlined in the previous section.[5] Their eigenfrequencies Ω_i are identified by finding zeros of $G(\Omega)$ in equation (7), and the corresponding

eigenvector components are given by

$$X_0^i = 1,$$
$$X_n^i = \frac{\omega_n^2}{\Omega_i^2 - \omega_n^2}. \tag{12}$$

Let us assume that we initiate our simulation by displacing the large oscillator by an amount $x_0(0)$ while keeping the small oscillators relaxed $x_n(0) = 0$ and all initial velocities at zero. In the new variables, the initial state of the system is given by the vector $\boldsymbol{X}(0)$, where $X_0 = \sqrt{M}x_0(0)$ and $X_n = \sqrt{m_n}x_0(0)$. The time evolution of the system is given by

$$\boldsymbol{X}(t) = \Sigma_{\Omega_i} \cos(\Omega_i t)(\boldsymbol{X}^i \cdot \boldsymbol{X}^i)^{-1} \left(\boldsymbol{X}(0) \cdot \boldsymbol{X}^i\right) \boldsymbol{X}^i. \tag{13}$$

Substituting the initial conditions, and the expression in equation (12) for the eigenvector components, we get

$$\boldsymbol{X}(t) = \sum_{\Omega_i} \cos(\Omega_i t) \frac{M + \sum_n [(m_n \omega_n^2)/(\omega_n^2 - \Omega_i^2)]}{M + \sum_n [(m_n \omega_n^4)/(\omega_n^2 - \Omega_i^2)^2]} \boldsymbol{X}^i. \tag{14}$$

The coordinate of the large oscillator is simply given by $x_0(t) = X_0(t)/\sqrt{M}$.

For the continuum of small modes, the above expansion breaks down, since the eigenvalue equation has no real solutions inside the continuum range. However, the edge modes are well defined, and they determine the dynamics at late times. Therefore, for the continuum case we can still write down the analogous expression which is valid only at late times:

$$\boldsymbol{X}(t) = \Sigma_{\Omega_{\mathrm{edge}}} \cos(\Omega_{\mathrm{edge}} t) \frac{\boldsymbol{X}(0) \cdot \boldsymbol{X}_{\mathrm{edge}}}{\boldsymbol{X}_{\mathrm{edge}} \cdot \boldsymbol{X}_{\mathrm{edge}}} \boldsymbol{X}_{\mathrm{edge}}. \tag{15}$$

The sums of equation (14) are replaced with the corresponding integrals, and we have the following expression for the displacement of the large oscillator at late times:

$$x_0(t) = x_0(0) \sum_{\Omega_{\mathrm{edge}}} \cos(\Omega_{\mathrm{edge}} t) \frac{M + \int d\omega \rho(\omega)[\omega_n^2/(\omega_n^2 - \Omega_{\mathrm{edge}}^2)]}{M + \int d\omega \rho(\omega)[\omega_n^4/(\omega_n^2 - \Omega_{\mathrm{edge}}^2)^2]}. \tag{16}$$

This expression is in excellent agreement with the numerical simulations. In the numerical example of Section 2.1, the upper edge mode dominates the late-time behaviour of the system, and its calculated contribution is plotted in Fig. 3, together with the numerically simulated motion.

2.4 The effect of viscosity

We now add an extra degree of realism by introducing viscous friction into the system. In MHD, continuum modes are spatially localized, and the effect of viscosity is to frictionally couple the neighbouring modes (see e.g. Hollweg 1987). In our simple model we introduce viscosity by adding frictional forces between the neighbouring oscillators:

$$f_{n,n+1} = -f_{n+1,n} = \gamma(\dot{x}_n - \dot{x}_{n+1}), \tag{17}$$

where $f_{n,n+1}$ is the force from the nth oscillator acting on the $(n+1)$th.

We now calculate how the system dissipates energy as a function of time. We will show that it occurs in two stages (see Fig. 6). (1) Initially, the small oscillators are strongly and simultaneously excited by the 'Landau-damped' large oscillator, then they become dephased, with the average relative motion between the neighbouring oscillators growing linearly in time. This leads to a very rapid dissipation of the bulk of the initial energy. (2) The edge modes
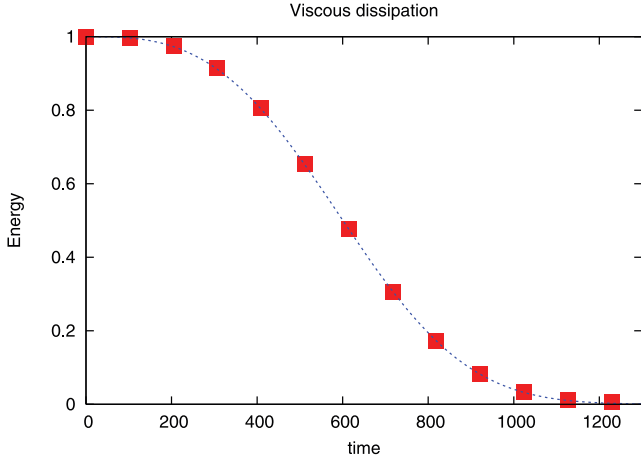
---

[4] There is a complex solution if the integration in the expression for $G(\Omega)$ is performed along the contour chosen according to the Landau rule. One then obtains a 'resonantly absorbed' or 'Landau-damped' mode (L07; Gruzinov 2008b), which exactly represents the exponential decay of stage (1) in our numerical experiment of the previous section.

[5] Alternatively, they can be found by diagonalizing the potential energy quadratic form.

Figure 6. The red squares show the viscous dissipation of the total energy during the numerical simulation. The dotted blue curve shows the analytical solution from equation (23).

persist, since the participating small oscillators move in phase and the energy dissipation is small. The energy of the modes is damped exponentially on a time-scale much longer than that of the first stage.

The dissipated energy is given by

$$W_{\text{diss}} = \Sigma_{n=1}^{N-1} \gamma (\dot{x}_{n+1} - \dot{x}_n)^2. \tag{18}$$

In the continuum limit, the small oscillators are labelled not by a discrete index n, but by a continuous variable λ. The expression for the dissipated energy is then

$$W_{\text{diss}} = \int d\lambda \, \tilde{\gamma} \left(\frac{\partial^2 x_\lambda(t)}{\partial \lambda \partial t} \right)^2, \tag{19}$$

where $\tilde{\gamma}$ is the viscous coefficient. After the initial exponential damping of the large oscillator and the excitation of the small oscillators, the latter initially move independently, with

$$x_\lambda(t) \simeq \tilde{x}(\lambda) \cos[\omega_\lambda t], \tag{20}$$

where $\tilde{x}(\lambda)$ is the amplitude of the λth oscillator. From the above equation, we then obtain

$$\left\langle \left(\frac{\partial^2 x_\lambda(t)}{\partial \lambda \partial t} \right)^2 \right\rangle = \frac{1}{2} \left\{ [d(\tilde{x}_\lambda \omega_\lambda)/d\lambda]^2 + \omega_\lambda^2 \tilde{x}_\lambda^2 (d\omega_\lambda/d\lambda)^2 t^2 \right\}, \tag{21}$$

where the $\langle \cdots \rangle$ stands for time averaging over many oscillation periods. For times $t \gg d\log x_\lambda/d\omega_\lambda$ the second term on the right-hand side of equation (21) dominates. For a simple model with $d\omega_\lambda/d\lambda = \text{const}$ and $\rho(\omega) = \text{const}$,

$$dE/dt \propto -At^2 E, \tag{22}$$

where E is the total energy of the system and $A = (\tilde{\gamma}/\rho)(d\omega_\lambda/d\lambda)$. The analytical solution for the energy and dissipated power,

$$E = E_0 \exp\left(-\frac{1}{3} A t^3\right), \tag{23}$$

$$W_{\text{diss}} = -\frac{dE}{dt} = At^2 E_0 \exp\left(-\frac{1}{3} A t^3\right),$$

agrees very well with numerical simulations; see Fig. 6. While the equations above were derived for restrictive assumptions ($d\omega_\lambda/d\lambda = \text{const}$ and $\rho(\omega) = \text{const}$), we found that the analytical formulae in equation (23) provide a good fit for a large variety of simulations.
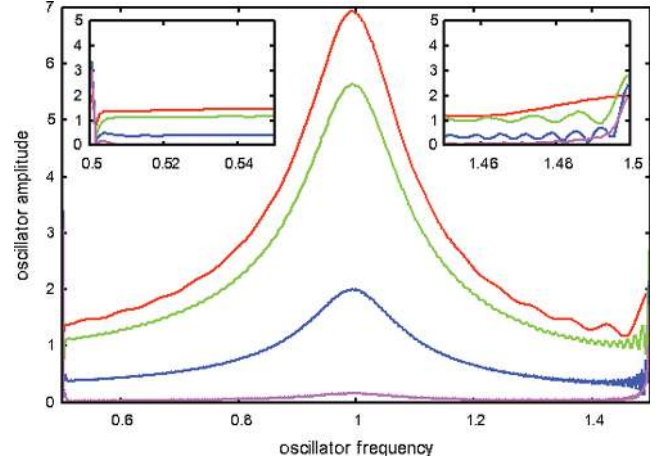

Figure 7. As in Fig. 4, this figure shows the amplitudes of the small oscillators at different times t. The energy of most oscillators is drained due to viscous dissipation. At late times, only the oscillators near the edges of the continuum have substantial energy.

This is because it is the small oscillators with the frequencies near that of the large oscillator which carry most of the energy, and in that narrow band our approximations hold.

After the energy dissipation due to dephasing is over, only the edge modes remain. This is illustrated in Fig. 7, where we show how the energies of the small oscillators evolve with time. At late times, only the oscillators taking part in the edge modes move substantially; this is because they remain in phase and do not dissipate much. At this stage the energy is drained by slow exponential decay of the edge modes.

3 TRANSIENT AND DRIFTING QPOS

Finite-size MHD systems feature a mix of continuum and discrete modes (see Poedts, Hermans & Goossens 1985, hereafter P85; GP). For axisymmetric field configurations the continuum modes occupy the whole flux surfaces and play an important role in the oscillatory dynamics; this was the motivation for L07 and our study of the previous section. We will argue in Section 5 that if the core field is highly tangled, the continuum modes become localized in space and discrete core modes will play a more important role. Thus it is important to study the case when the crustal modes are coupled to a set of discrete core modes. In this section we show that if the frequencies of the discrete modes are regularly spaced in some frequency intervals, then the system displays *transient QPOs* that are entirely missed by its normal-mode analysis. This is interesting from the observational point of view, since many of the observed magnetar QPO features are transient.

Suppose that a set of discrete modes are located in the interval $\Delta\omega$ around frequency ω_0 and are separated by a regular frequency interval $\delta\omega$, and assume the following hierarchy:

$$\delta\omega \ll \Delta\omega \ll \omega_0. \tag{24}$$

After the modes are excited, they are initially in phase but will dephase rapidly on the time-scale $1/\Delta\omega$. However, at times $t_n = 2\pi n/\delta\omega$ the modes come into phase again and pull coherently on the large oscillator. Therefore, a transient QPO feature should appear around these times at a frequency close to ω_0. In Figs 8 and 9 we show the dynamical spectrum from a simulation where the model was designed to produce QPOs at two specific frequencies. The transient QPOs agree well with the expectations. As is seen from the
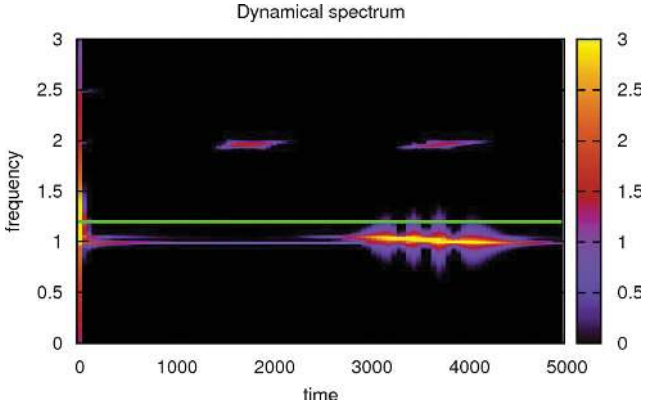
Figure 8. Dynamical spectrum from a simulation where we have designed the continuum so as to produce transient QPOs at frequencies $\omega = 1$ and 2 (the coloured scale denotes log (power)). The green horizontal line denotes the frequency of the large oscillator ($\Omega = 1.2$).
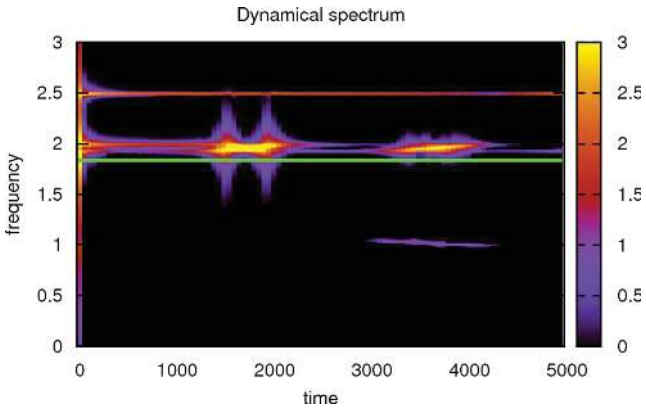

Figure 9. Dynamical spectrum from a simulation with a continuum that is identical to the one of Fig. 8. We have shifted the frequency of the large oscillator, denoted by the green horizontal line, to $\Omega = 1.8$. By comparison with Fig. 8 it is clear that the drifting QPOs at $\omega = 2$ are now much stronger as they are closer to the large oscillator frequency. Note that the edge mode at $\omega = 2.5$ is clearly visible.

figures, the strongest transient QPOs are those whose frequencies are the closest to that of the large oscillator; this is because the response of the large oscillator is the strongest around its proper frequency.

One can now easily understand the frequency drifts in fig. 10 of L07 (Fig. 10 in this paper) as an artefact of the discrete sampling of the continuum. In the simulations of that paper, the core continuum was sampled with a set of densely and regularly placed Alfvén modes by slicing the field into finite-width flux shells. The spacing $\delta\omega$ between the modes was not constant but a function of the Alfvén frequency ω. In that case, the QPO drifts with the QPO frequency $\omega(t)$ given by the inverse relation

$$t(\omega) = \frac{2\pi n}{\delta\omega(\omega)}. \tag{25}$$

With this relation we are able to fit all of L07 drifting QPOs, as shown in Figs 10 and 11. Note that multiple QPOs correspond to different branches of the Alfvén continuum. As expected, the drifting QPOs are amplified near the crustal frequencies, since there the response of the crust to the core modes' pull is the strongest.
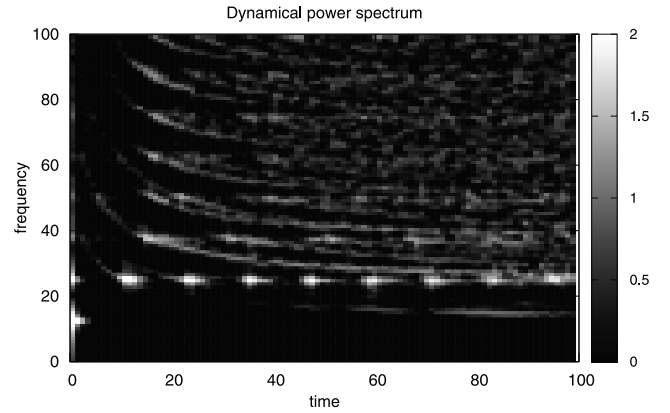

Figure 10. Dynamical power spectrum of the spherical magnetar model from L07. The grey-scale denotes log (power).
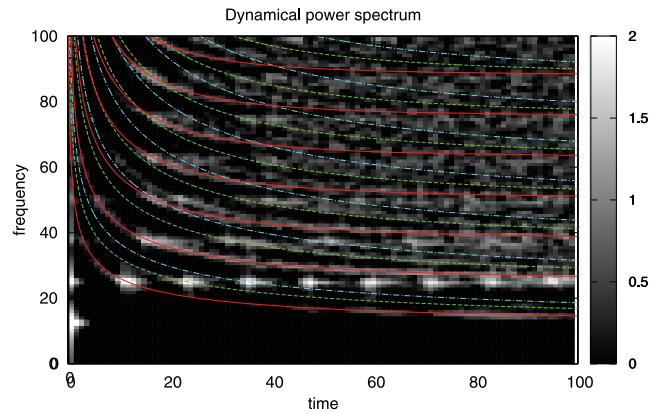

Figure 11. We have used equation (25) to fit the drifting QPOs from Fig. 10. The red curves are $n = 1$ drifts, green curves are $n = 2$ and blue curves are $n = 3$. The higher frequency drifts originate from Alfvén overtones.

4 MORE REALISTIC MAGNETAR MODELS

In this section we extend the constant magnetic field and constant density magnetar model from L07 to include more realistic pressure and density profiles and more general (but still axisymmetric) magnetic field configurations. Our aim is to use this model to (1) calculate numerically Alfvén eigenmodes and their eigenfrequencies on different flux surfaces inside the star, in order to determine the continuous spectrum of the fluid core, and (2) use these modes to simulate the dynamics of a realistic magnetar. In order to calculate the Alfvén eigenmodes and eigenfrequencies for a realistic magnetar model, we employ the linearized equations of motion for an axisymmetric magnetized, self-gravitating plasma. The general equations, which are derived in detail in P85 and given in their equations (53) and (54), constitute a fourth-order system of coupled ordinary differential equations in the case of a mixed poloidal and toroidal magnetic field. The formalism of P85 is briefly summarized in Appendix B. In the case of a purely poloidal magnetic field, the system simplifies to two uncoupled second-order differential equations (P85, equations 70 and 71).

4.1 The model

We assume our star is non-rotating and neglect its deformation due to the magnetic pressure, which is expected to be small. Therefore, we consider a spherically symmetric background model that is a

solution of the Tolman–Oppenheimer–Volkoff equation (TOV equation).[6] The hydrostatic equilibrium is calculated using a SLy equation of state (Douchin & Haensel 2001; Haensel & Potekhin 2004; Haensel, Potekhin & Yakovlev 2007), which can be found in tabulated form on the website http://www.ioffe.ru/astro/NSG/NSEOS/. The integration of the TOV equation is performed using a fourth-order Runge–Kutta scheme, integrating from the centre of the star outward until we reach a mass density $\rho = 1.3 \times 10^{14}\,\mathrm{g\,cm^{-3}}$, which is consistent with the crust–core interface in the equation of state from Douchin & Haensel (2001). The resulting model has a central mass density $\rho_{\mathrm{c}} = 10^{15}\,\mathrm{g\,cm^{-3}}$, a total mass of $1.40\,\mathrm{M_\odot}$ and a radius of $R_{\mathrm{core}} = 1.07 \times 10^6\,\mathrm{cm}$. To this spherical model we add a poloidal magnetic field, which we generate by placing a circular current loop of radius a and current I around the centre of the star. The field is singular near the current loop, however, all the field lines which connect to the crust (and thus are physically related to observable oscillations) carry finite field values. This particular field configuration is chosen as an example; there is an infinite number of ways to generate poloidal field configurations. In Appendix B we will add to this field a toroidal component and calculate the corresponding Alfvén continuum of the core.

4.2 The continuum

In order to find the equations of motion for the magnetized material in the neutron star core, we would need to add self-gravity to the ideal MHD equations. This problem has been solved by P85 in a tour the force mathematical approach. In that paper the authors assume a self-gravitating axisymmetric equilibrium with a field geometry consisting of mixed poloidal and toroidal field components, and they derive linearized equations of motion. For this field geometry it is convenient to work with so-called flux coordinates (ψ, χ, ϕ).[7] The basic concept behind this curvilinear coordinate system is the magnetic flux surface, which is defined as the surface perpendicular to the Lorentz force $\boldsymbol{F}_{\mathrm{L}} \propto \boldsymbol{j} \times \boldsymbol{B}$. From this definition it is clear that the magnetic field lines lie in flux surfaces. If one considers a closed loop on a flux surface which makes one revolution around the axis of symmetry, then the magnetic flux ψ through the loop depends on the flux surface only and is the same for all of the loops. Therefore ψ is chosen as the coordinate labelling the flux surfaces. In each flux surface we can denote a position by its azimuthal angle ϕ and its 'poloidal' coordinate χ, which is defined as the length along $\phi = \mathrm{const}$ line. In P85, it is shown that the equations of motion allow for a class of oscillatory solutions that are located on singular flux surfaces, constituting a continuum of eigenmodes and eigenfrequencies. In the case of a purely poloidal field ($B = B_\chi$), the continuum solutions are degenerate and polarized either parallel (ξ_χ) or perpendicular (ξ_ϕ) to the magnetic field lines. In the latter case the displacement is ϕ independent. It is clear that in contrast to the χ-polarized modes, the ϕ-polarized modes are purely

horizontal and are therefore unaffected by gravity. This latter case is considered here.

The equation of motion is in this case simply the Alfvén wave equation:

$$\frac{\partial^2 \xi_\phi(\psi, \chi)}{\partial t^2} = F\left[\xi_\phi(\psi, \chi)\right], \tag{26}$$

where the operator F is given by

$$F\left[\xi_\phi(\psi, \chi)\right] = \frac{B}{4\pi x \rho}\frac{\partial}{\partial \chi}\left[x^2 B \frac{\partial}{\partial \chi}\left(\frac{\xi_\phi(\psi, \chi)}{x}\right)\right]. \tag{27}$$

Here x is the distance to the magnetic axis of symmetry. Although in the presence of a mixed poloidal and toroidal field the equations still give rise to a continuous set of solutions, the calculations are significantly complicated as the continuum modes are affected by the toroidal component of the field, by gravity and by compressibility. For the sake of simplicity we will ignore toroidal fields in our dynamic simulations. We will, however, calculate the continuum frequencies for a mixed poloidal and toroidal field in Appendix B.

For determining the spectrum of the core continuum, the appropriate boundary conditions are $\xi_\phi(\chi = \chi_{\mathrm{c}}) = 0$, where $\chi_{\mathrm{c}}(\phi)$ marks the location of the crust–core interface. The full significance of this boundary condition will become apparent in later in this section when we develop the analysis for the crust–core interaction. With this boundary condition, equation (26) constitutes a Sturm–Liouville problem on each separate flux surface ψ. Using the stellar structure model and magnetic field configuration from Section 4.1, we can calculate the eigenfunctions and eigenfrequencies for each flux surface ψ. The reflection symmetry of the stellar model and the magnetic field with respect to the equatorial plane assures that the eigenfunctions of equation (26) are either symmetric or anti-symmetric with respect to the equatorial plane. We can therefore determine the eigenfunctions by integrating equation (26) along the magnetic field lines from the equatorial plane $\chi = 0$ to the crust–core interface $\chi = \chi_{\mathrm{c}}(\psi)$. Let us consider the odd modes here for which $\xi_\phi(0) = 0$, and solve equation (26) with the boundary condition $\xi_\phi(\chi_{\mathrm{c}}) = 0$ at the crust–core interface; for even modes, the boundary condition is $\mathrm{d}\xi_\phi(0)/\mathrm{d}\chi = 0$. We find the eigenfunctions by means of a shooting method; using fourth-order Runge–Kutta integration we integrate from $\chi = 0$ to χ_{c}. The correct eigenvalues σ_n and eigenfunctions $\xi_n(\chi)$ are found by changing the value of σ until the boundary condition at ξ_n is satisfied. In this way we gradually increase the value of σ until the desired number of harmonics is obtained. In Fig. 12 we show a typical resulting core continuum.

According to Sturm–Liouville theory the normalized eigenfunctions ξ_n of equation (26) form an orthonormal basis with respect to the following inner product:

$$\langle \xi_m, \xi_n \rangle = \int_0^{\chi_{\mathrm{c}}} r(\chi)\,\xi_m(\chi)\,\xi_n(\chi)\,\mathrm{d}\chi = \delta_{m,n}, \tag{28}$$

where $\delta_{m,n}$ is the Kronecker delta and $r = 4\pi\rho/B_\chi$ is the weight function. We have checked that the solutions we find satisfy the orthogonality relations.

We are now ready to compute the coupled crust–core motion. Here we follow L07 and assume that the crust is an infinitely thin elastic shell.[8] We label the latitudinal location by the flux surface

---

[6] Note that although our background equilibrium model is based on the relativistic TOV equation, our equations of motion will be derived using classical MHD.

[7] There exists a variety of magnetic coordinate systems that can be used to study axisymmetric MHD equilibria. A useful overview of systems used by plasma and MHD physicists is given in Alladio & Micozzi (1996). In Colaiuda et al. (2009), the authors employ an alternative relativistic system of coordinates for their study of torsional Alfvén oscillations of magnetars, which allows them to reduce the 1+2 dimensional evolution equation for magnetar oscillations to a 1+1 dimensional form.
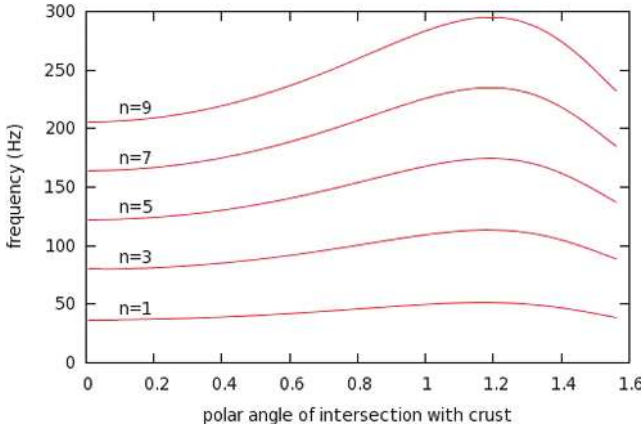
[8] It is straightforward to relax this assumption, and carry out the analysis of this section for the finite crustal thickness. However, from Section 2 it is clear that the interesting dynamics is dominated by the spectral structure of the core Alfvén waves; therefore, in order to flesh out the physics we choose the simplified model of the crust.

Figure 12. The red curves show the Alfvén frequencies σ_n as a function of the angle $\theta(\psi)$, the polar angle at which the flux surface ψ intersects the crust. Since we are only considering odd crustal modes, the only Alfvén modes that couple to the motion of the star are the ones with an odd harmonic number n. This particular continuum was calculated using a poloidal field with an average surface value $B_{surface} \sim 6 \times 10^{14}$ G, generated by a circular ring current of radius $a = R_*/2$.

ψ intersecting the crust, and consider the crustal axisymmetric displacements $\bar{\xi}_\phi(\psi)$. In the MHD approximation, the magnetic stresses enforce a no-slip boundary condition at the crust–core interface, such that $\xi_\phi(\psi, \chi_c) = \bar{\xi}_\phi(\psi, \chi_c)$ instead of $\xi_\phi(\psi, \chi_c) = 0$. It is useful to make the following substitution:

$$\zeta(\psi, \chi) \equiv \xi_\phi(\psi, \chi) - \bar{\xi}_\phi(\psi)\, w(\psi, \chi), \tag{29}$$

where we choose the function $w(\psi, \chi)$ so that (a) it corresponds to the static displacement in the core and hence satisfies $F(w(\psi, \chi)) = 0$, and (b) $w(\psi, \chi_c) = 1$. Therefore the new quantity satisfies the boundary condition $\zeta(\psi, \chi_c) = 0$ and can be expanded into the Alfvén normal modes ξ_n which satisfy the same boundary conditions.

We now proceed by substituting equation (29) into equation (26) thus obtaining a simple equation of motion for ζ:

$$\frac{\partial^2 \zeta(\psi, \chi)}{\partial t^2} - F(\zeta(\psi, \chi)) = -w(\psi, \chi)\frac{\partial^2 \bar{\xi}_\phi(\psi)}{\partial t^2}. \tag{30}$$

From the definition of the operator F it follows that for the odd modes

$$w(\psi, \chi) = x(\psi, \chi)\int_0^\chi \frac{K(\psi)}{x^2(\psi, \chi')\, B_\chi(\psi, \chi')}\,d\chi'. \tag{31}$$

Here the constant $K(\psi)$ is chosen such that $w(\psi, \chi_c) = 1$, in order that $\zeta = 0$ on both boundaries. We expand ζ and w into a series of ξ_ns:

$$\zeta(\psi, \chi, t) = \sum_n a_n(\psi, t)\, \xi_n(\psi, \chi), \tag{32}$$

$$w(\psi, \chi) = \sum_n b_n(\psi)\, \xi_n(\psi, \chi), \tag{33}$$

equation (30) reduces to the following equations of motion for the eigenmode amplitudes a_n:

$$\frac{\partial^2 a_n(\psi)}{\partial t^2} + \sigma_n^2(\psi)\, a_n(\psi) = -b_n(\psi)\frac{\partial^2 \bar{\xi}_\phi}{\partial t^2}. \tag{34}$$

These equations show how the core Alfvén modes are driven by the motion of the crust. To close the system, we must address the motion of the crust driven by the hydromagnetic pull from the core.

The equation of motion for the crust is given by

$$\frac{\partial^2 \bar{\xi}_\phi}{\partial t^2} = L_{el}(\bar{\xi}_\phi) + L_B, \tag{35}$$

where the acceleration due to elastic stresses L_{el} is

$$L_{el}(\bar{\xi}_\phi) = \omega_{el}^2\left[\frac{\partial^2 \bar{\xi}_\phi}{\partial \theta^2} + \cot(\theta)\frac{\partial \bar{\xi}_\phi}{\partial \theta} - (\cot(\theta)^2 - 1)\,\bar{\xi}_\phi\right], \tag{36}$$

where θ is the polar angle (cf. L07). The acceleration L_B due to the magnetic stresses between the crust and the core can be expressed as

$$L_B = -\frac{x B^2}{4\pi\Sigma}\cos\alpha\,\frac{\partial}{\partial \chi}\left(\frac{\xi_\phi}{x}\right)_{\chi=\chi_{crust}}, \tag{37}$$

where x is the distance to the axis of the star, Σ is column mass density of the crust and α is the angle between the magnetic field line and the normal vector of the crust.

It is convenient to express the crustal displacement $\bar{\xi}_\phi$ as a Fourier series, being a sum normal modes of the free-crust problem. Using equation (36) is straightforward to show analytically that the eigenfunctions f_l of the free-crust problem (equation 35 with $L_B = 0$) are

$$f_l(\theta) \propto \frac{dY_{l0}(\theta)}{d\theta}, \tag{38}$$

with eigenfrequencies

$$\omega_l = \omega_{el}\sqrt{(l-1)(l+2)}. \tag{39}$$

Here Y_{l0} is the $m = 0$ spherical harmonic of degree l. The normalized functions f_l form an orthonormal basis, so that

$$\int_0^\infty f_l(\theta)\, f_m(\theta)\sin(\theta)\,d\theta = \delta_{l,m}, \tag{40}$$

where $\delta_{l,m}$ is again the Kronecker delta. The crustal displacement can then be expressed in terms of f_l:

$$\bar{\xi}_\phi(\theta, t) = \sum_l c_l(t)\, f_l(\theta). \tag{41}$$

Substituting equation (41) into equation (35) we obtain the equations of motion for the crustal mode amplitudes c_l:

$$\frac{\partial^2 c_l}{\partial t^2} + \omega_l^2 c_l = \int_0^\pi L_B(\theta, t)\, f_l(\theta)\sin\theta\,d\theta. \tag{42}$$

We can express L_B as

$$L_B(\psi, t) = -\frac{B_\chi^2(\psi)}{4\pi\Sigma}\cos(\alpha(\psi))\left[\sum_n a_n(t)\frac{\partial \xi_n(\psi)}{\partial \chi}\right.$$
$$\left. + \frac{K(\psi)}{x(\psi)B(\psi)}\sum_k c_k(t)\, f_k(\theta(\psi))\right]_{\chi=\chi_c}. \tag{43}$$

Up to this point the derived equations of motion for the crust and the fluid core are exact. We are now ready to discretize the continuum by converting the integral of equation (42) into a sum over N points θ_i. In order to avoid the effect of phase coherence (see Section 3) which caused drifts in the results from L07, we sample the continuum randomly over the θ interval $[0, \pi/2]$. In the following, functional dependence of the coordinate ψ or $\theta(\psi)$ is substituted

by the discrete index i which denotes the ith flux surface:

$$\frac{\partial^2 c_l}{\partial t^2} + \omega_l^2 c_l = 2 \sum_i L_B(\theta_i, t) f_{il} \sin \theta_i \Delta \theta_i$$

$$= - \sum_i \sin(\theta_i) \Delta \theta_i f_{il} \left[\frac{B_{\chi,i}^2}{2\pi \Sigma} \cos(\alpha_i) \left(\sum_n a_{in} \frac{\partial \xi_{in}}{\partial \chi} \right. \right.$$

$$\left. \left. + \frac{K_i}{x_i B_{\chi,i}} \sum_k c_k f_{ik} \right) \right]_{\chi=\chi_c}, \tag{44}$$

$$\frac{\partial^2 a_{in}}{\partial t^2} + \sigma_{in}^2 a_{in} = -b_{in} \sum_l \frac{\partial^2 c_l}{\partial t^2} f_{il}. \tag{45}$$

These are the equations that fully describe dynamics of our magnetar model. As with the toy model from Section 2 we integrate them using a second-order leapfrog scheme which conserves the total energy to high precision. As a test we keep track of the total energy of the system during the simulations. Further we have checked our results by integrating equations (44) and (45) with the fourth-order Runge–Kutta scheme and found good agreement with leapfrog integration.

4.3 Results

Based on our Section 2 results, we have a good idea of what type of dynamical behaviour should occur in our more realistic magnetar model. First, we expect that crustal modes with frequencies inside the Alfvén continuum will be damped quickly by resonant absorption ('Landau-damping' in the terminology of Gruzinov 2008b). Second, as with our previous model we expect the late-time behaviour of the system to show QPOs near the edges of the continuum, or edge modes. The third important feature of our model is that the continuum may possibly contain gaps, as is shown in Fig. 13. In this case there is the possibility that crustal frequencies fall inside the gaps and remain undamped. In all of our simulations these expectations have come true. We will now show the results from a simulation which illustrate the above-mentioned effects.

The basic freedom of choice that we have for our model is the strength and geometry of the equilibrium magnetic field. We choose here a purely poloidal magnetic field with an average strength at the surface of $B_{\text{surf}} = 10^{15}$ G, induced by a circular current loop of radius $a = 0.5R_*$. This field gives us a gap in the continuum at frequencies $53 < \omega < 78$ Hz.
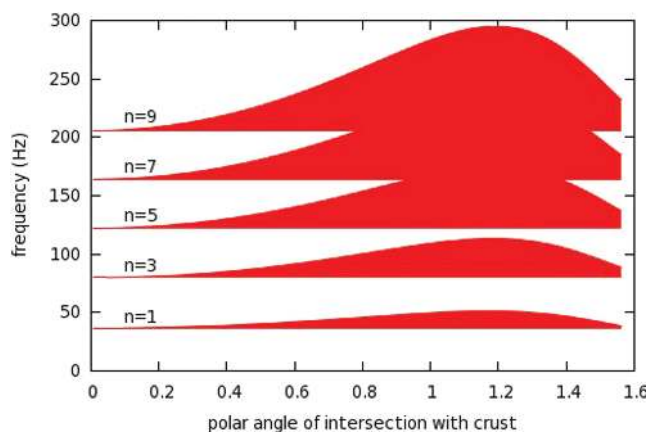

Figure 13. After filling the curves from Fig. 12, 'gaps' in the continuum become visible around $\sigma \sim 70$ and ~ 120 Hz.
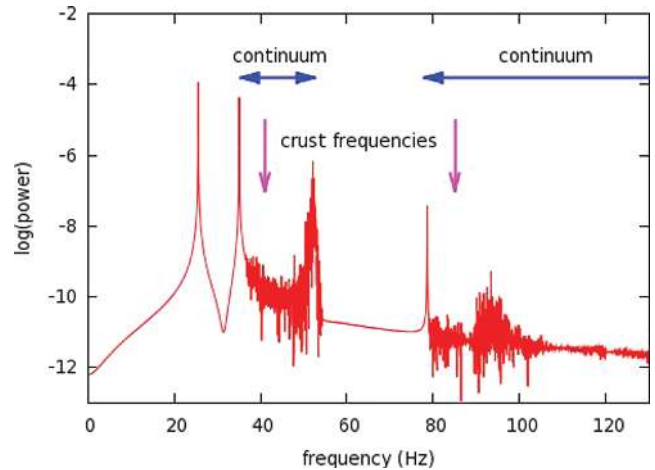

Figure 14. Power spectrum of the crustal dynamics for a magnetar with a single 'gap' in the Alfvén continuum. In this case the crustal frequencies are within the continuum, causing the crust modes to be Landau damped.

We consider the lowest degree odd crustal modes with frequencies $\omega_2 = 40$ Hz and $\omega_4 = 84.5$ Hz, which we couple to 5000 continuum oscillators (the Alfvén continuum). We sample the continuum at 1000 randomly chosen flux surfaces, and at each flux surface we consider five Alfvén overtones.

As with our toy model from Section 2, we initiate the simulation by displacing the crust ($c_2 = c_4 = 1$) while keeping the continuum oscillators (the Alfvén modes) relaxed ($a_{in} = 0$).

In Figs 14 and 15 we show the resulting power spectrum for two different models. In the first one, the crustal frequencies are located inside the core continuum range, and the peaks due to the edge modes appear. By contrast, in the second case one of the crustal frequencies belongs to the gap, and a peak representing the global gap mode stands strongly above the background. We note that the gap-mode's frequency lies close to but does not coincide with the crustal-mode frequency; we found this to be a generic feature of our models, with the difference of 10 per cent for the typical model parameters. The gap modes are particularly interesting because they have relatively large amplitudes, and are not as strongly damped by viscosity as the edge modes.
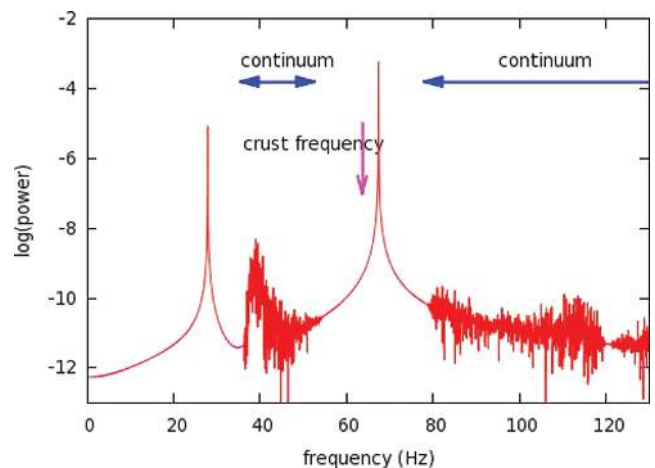

Figure 15. Power spectrum of the crustal dynamics for a magnetar with a single 'gap' in the Alfvén continuum. The global mode within the gap is not damped, and its frequency is similar, but not identical, to that of the crustal mode in the same gap.

It must be emphasized that for all persistent modes in the system, the position in the frequency space of the core Alfvén continuum plays the key role in setting the global-mode frequency and in determining its longevity.

We note that Lee (2008) has used a different method to identify discrete modes in a magnetar with similar magnetic configuration to ours. These modes were not associated with crustal frequencies, and we strongly suspect that they were located in the gaps of the continuum spectrum and could be identified with the edge or gap modes presented in this work.

5 TANGLED MAGNETIC FIELDS

Our preceding discussion of the continuum was predicated on the foliation of the axisymmetric magnetic field into the flux surfaces, with each of the singular continuum mode localized on the flux surfaces. These modes are 'large' – they are coherent over the spatial extent comparable to the size of the system, and thus they play an important role in the overall dynamics – they are responsible for the resonant absorption of the crust oscillations, and contribute to generating the edge and gap modes. However, what happens if the field cannot be foliated into the flux surfaces, but is instead tangled in a complicated way? One can argue that the continuum part of the spectrum still persists, as follows.

Consider an arbitrary field line anchored at the crust–core interface at both ends, and choose a tube of field lines of infinitesimal radius which is centred on the original field line (see Fig. 16). It is clear that a twisting Alfvén mode exists in the tube: it is obtained by the circular rotation of the fluid around the central field line, propagating along the central field line with the local Alfvén velocity. Since there is a continuum of the field-line lengths, there is also a continuum of Alfvén modes. However, the modes we constructed are highly localized in space and have a small leverage in the overall dynamics. We conjecture that the more tangled the fields are, the less role do the singular continuum modes play in the overall dynamics.

Whilst we cannot rigorously prove this conjecture, we can motivate it as follows: consider an area element δS of random orientation with the normal $\hat{n}$ inside the star, and consider a shearing motion along the element. This shearing motion will be resisted by the $B_{\hat{n}}$ component of the magnetic field, with the effective shear modulus of order

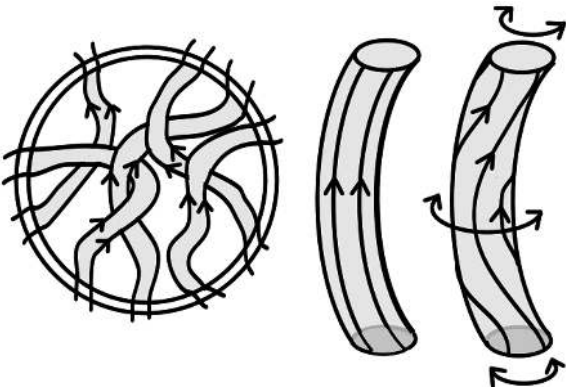$$\mu_{\text{eff}} \sim \frac{\langle B_{\hat{n}}^2 \rangle}{4\pi}, \tag{46}$$

Figure 16. Schematic illustration of tangled a magnetic field inside a magnetar. Locally, the field consists of flux tubes which contain a continuum of twisting Alfvén modes.

where $\langle \cdots \rangle$ stands for averaging over the area element. For ordered field, it is possible to choose the orientation of the area element so that $\mu_{\text{eff}} \simeq 0$; the presence of such an orientation makes a fundamental difference between MHD and elasticity theory and is responsible for the presence of continuous spectrum in MHD. However, if the linear size of the δS is greater than the characteristic length on which the field is tangled, then μ_{eff} is non-zero for all orientations of $\hat{n}$. Therefore, for highly tangled fields there can be no large-scale singular continuum modes, and their existence is restricted to the small scales. Hence our assertion that for strongly tangled fields continuum modes play a secondary dynamical role.

One is then faced with the problem when crustal modes are coupled to a set of discrete core Alfvén modes. In Appendix A we show how to find the eigensolution of such a problem, provided that all of the coupling coefficients are known.

How does one quantify the degree to which the fields are tangled? Some insight comes from the numerical simulations of Braithwaite and colleagues, who have studied what type of fossil fields remain in a stratified star after an initial period of fast relaxation. Consider a stable fossil field configuration, such as the one obtained in the simulations of Braithwaite & Spruit (2004) and Braithwaite & Nordlund (2006) (see also Gruzinov 2008a for analytical considerations). There, the final field is nearly, but not perfectly axisymmetric and has a small-scale random component. For a less centrally concentrated initial field, Braithwaite (2008) shows that the final fossil field is in general non-axisymmetric and can have a complicated topology.[9]

As a starting point, we shall consider the nearly axisymmetric field with a small random component. The latter acts like a small extra shear modulus μ_{eff} and dynamically couples the flux surfaces of the axisymmetric component. We then quantify the degree of tangling by the relative value of μ_{eff} and $B^2/(4\pi)$.

5.1 Simple model: 'square' neutron star

To study this idea further, we specify a very simple model of a neutron star, motivated by the one considered in L06, see Fig. 17 that nevertheless captures the essential physics.

Consider a perfectly conducting homogeneous fluid of density ρ contained in a box with width L_x, length L_y and depth L_z. The magnetic field in this box is everywhere aligned with the y-axis and its strength is a function of x only. We assume that gravity is zero and consider a Lagrangian displacement $\xi(x, y, t)$ of the fluid along the z-direction; we specify periodic boundary conditions in this direction (one should think of the z-direction as azimuthal). We now add to this model a small effective shear modulus μ_{eff} due to the field tangling. The fluid equation of motion is

$$\frac{\partial^2 \xi}{\partial t^2} = c_A^2(x) \frac{\partial^2 \xi}{\partial y^2} + c_s^2 \nabla^2 \xi. \tag{47}$$

Here $c_A(x)$ is the Alfvén velocity and $c_s = \sqrt{\mu_{\text{eff}}/\rho}$ is the μ_{eff}-generated shear velocity. If we assume a small shear speed, i.e. $c_s \ll c_A$, equation (47) reduces to

$$\frac{\partial^2 \xi}{\partial t^2} = c_A^2(x) \frac{\partial^2 \xi}{\partial y^2} + c_s^2 \frac{\partial^2 \xi}{\partial x^2}. \tag{48}$$

---

[9] Gruzinov (2009) demonstrates that even this situation is not the most general. He finds that the relaxed field generally has multiple current sheets, and argues that the global field relaxation is dominated by the dissipation within these singular layers. The details do not concern us for the purposes of this paper.
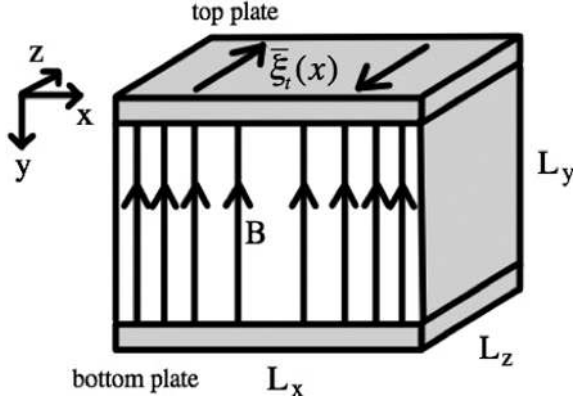
Figure 17. Schematic illustration of the box model. Perfectly conducting incompressible fluid is sandwiched between perfectly conducting top and bottom plates. The box is periodic in *z*-direction and the displacements of the plates (crust) are in the *z*-direction. The magnetic field is directed along *y*-axis and its strength varies as a function of *x*.

We now find the core Alfvén eigenmodes. After adapting the no-slip boundary conditions,

$$\xi\left(-\frac{L_x}{2}, y, t\right) = \xi\left(\frac{L_x}{2}, y, t\right) = 0,$$

$$\xi\left(x, -\frac{L_y}{2}, t\right) = \xi\left(x, \frac{L_y}{2}, t\right) = 0, \tag{49}$$

the problem can be easily solved by separation of variables $\xi(x, y, t) \propto e^{i\omega t} \sin\{\pi m[(y/L_y) + 1/2]\} X(x)$, where $m = 1, 2, \ldots$. Plugging this in equation (48) we find for the *x*-dependent part of the solution:

$$c_s^2 \frac{\partial^2 X}{\partial x^2} = \left[\omega^2 - \omega_{A,m}^2(x)\right] X. \tag{50}$$

Here $\omega_{A,m}(x) = \pi m c_A(x)/L_y$ can be interpreted as the frequency of the *m*th Alfvén overtone at *x*. From the above expression it is clear that in the limit of very small c_s, the solution for *X* must be close to zero everywhere except in a very small neighbourhood of $\omega_{A,m}(x) = \omega$. It is in this limit that the solutions are located on singular flux surfaces. However, in the presence of the non-vanishing shear velocity c_s, the eigenmodes spread out on neighbouring field lines, effectively coupling the motion on different flux surfaces. The continuum of Alfvén frequencies $\omega_{A,m}(x)$ will in this case be no longer solutions of the system. Instead, the coupling term gives rise to a discrete set of solutions rather than a continuum. Equation (50) is the mathematical equivalent of Schrödingers equation, which can in general cases be solved numerically. However, for many special case exact solutions exist. Let us consider, for the sake of simplicity, a field configuration in our box such that

$$c_A^2(x) = a_{c_A} x^2 + c_{A,0}^2. \tag{51}$$

We can rewrite equation (50) as follows:

$$c_s^2 \frac{\partial^2 X}{\partial x^2} = -\frac{\pi^2 m^2 a_{c_A}}{L_y} x^2 X + \left(\omega_m^2 - \frac{\pi^2 m^2 c_{A,0}^2}{L_y}\right) X. \tag{52}$$

This differential equation is the mathematical equivalent of the quantum harmonic oscillator problem for which the exact solution is well known. The eigenfrequencies are given by

$$\omega_{mn}^2 = \pi(1 + 2n) m c_s \sqrt{a_{c_A}}/L_y + c_{A,0}^2 \pi^2 m^2/L_y. \tag{53}$$

Here $n\,(= 0, 1, \ldots)$ is the 'quantum' number labelling the harmonic-oscillator wavefunctions. We see that instead of a continuum, we
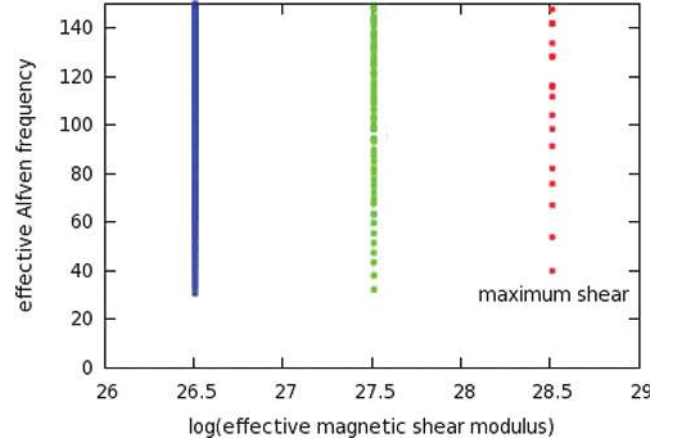

Figure 18. Alfvén frequencies as a function of the effective magnetic shear modulus. As one decreases the shear, the spectrum tends to a continuum.

obtain a densely packed discrete set of frequencies with the frequency spacing $\omega_{m,n} - \omega_{m,n-1} \sim \pi m c_s \sqrt{a_{c_A}}/L_y \omega_{m,n}$.

With the no-slip boundary conditions on the left- and right-hand sides $x = \pm L_x/2$, the eigenvalue equation must be solved numerically. An example of such calculation is shown in Fig. 18. There, the spacing between the discrete Alfvén modes is shown to increase as one increases the effect of the field tangling characterized by the μ_{eff}.

We now introduce the crustal modes into the problem by making the top and bottom of the box elastic and mobile. We allow their displacement $\bar{\xi}_{t,b}(x, t)$ in the *z*-direction, and impose the boundary conditions on the sides:

$$\bar{\xi}_{t,b}(-L_x/2, t) = \bar{\xi}_{t,b}(L_x/2, t) = 0. \tag{54}$$

Here the subscripts 't' and 'b' stand for the top and bottom of the box, respectively. The top and bottom are assumed to be thin and have mass M_{cr} and surface density $\sigma = M_{\mathrm{cr}}/(L_x L_z)$. The crustal equation of motion is given by

$$\frac{\partial^2 \bar{\xi}_t}{\partial t^2} = v_s^2 \frac{\partial^2 \bar{\xi}_t}{\partial x^2} - \frac{\{B_z B_x\}_t}{4\pi\sigma},$$

$$\frac{\partial^2 \bar{\xi}_b}{\partial t^2} = v_s^2 \frac{\partial^2 \bar{\xi}_b}{\partial x^2} + \frac{\{B_z B_x\}_b}{4\pi\sigma}, \tag{55}$$

where v_s is the shear velocity in the crust. The crustal angular frequencies are given by $\omega_j^{\mathrm{cr}} = j\pi v_s/L_y$ with the corresponding crustal mode eigenfunctions $\bar{\xi}_j = \sin\{j\pi[(x/L_x) + 1/2]\}$, where $j = 1, 2, \ldots$ is roughly equivalent to *l* in the spherical case. The symmetry of the problem allows one to consider either symmetric $\bar{\xi}_t = \bar{\xi}_b$ or antisymmetric $\bar{\xi}_t = -\bar{\xi}_b$ crustal modes. This will couple to the symmetric ($m = 1, 3, 5, \ldots$) or antisymmetric ($m = 2, 4, 6, \ldots$) Alfvén modes of the core.

Just as in Section 4, it is now convenient to define a new variable $\zeta(x, y, t)$ for the core displacement:

$$\zeta(x, y, t) = \xi(x, y, t) - \xi_0(x, y, t), \tag{56}$$

where

$$\xi_0(x, y, t) = \frac{1}{2}\left(\bar{\xi}_t(x, t) + \bar{\xi}_b(x, t)\right)$$
$$+ \left(\bar{\xi}_t(x, t) - \bar{\xi}_b(x, t)\right)\frac{y}{L_y}. \tag{57}$$

The new variable observes the regular boundary condition $\zeta = 0$ on all the box edge, and satisfies the following inhomogeneous partial

differential equation:

$$\left(\frac{\partial^2}{\partial t^2} - c_A^2(x)\frac{\partial^2}{\partial y^2} - c_s^2\frac{\partial^2}{\partial x^2}\right)\zeta(x, y, t) = g(x, y, t), \qquad (58)$$

where

$$g(x, y, t) = -\left(\frac{\partial^2}{\partial t^2} - c_s^2\frac{\partial^2}{\partial x^2}\right)\xi_0(x, y, t). \qquad (59)$$

The advantage of the new variable is that it satisfies the regular boundary condition $\zeta = 0$ on all the boundaries of the box. It can therefore be expanded as a series consisting of eigenfunctions ξ_{mn} of the right-hand side of equation (48):

$$\zeta(x, y, t) = \Sigma_{mn}a_{mn}(t)\xi_{mn}(x, y). \qquad (60)$$

The rest of the procedure is very similar to that in Section 4. We expand the crustal displacement into a series consisting of the eigenmode wavefunctions $\bar{\xi}_j$:

$$\bar{\xi}_t(x, t) = \Sigma_j p_j(t)\bar{\xi}_j(x),$$
$$\bar{\xi}_b(x, t) = \Sigma_j q_j(t)\bar{\xi}_j(x), \qquad (61)$$

where $p_j(t)$ and $q_j(t)$ are real numbers. The magnetar deformation is now fully represented by a set of generalized coordinates $[p_j(t), q_j(t), a_{mn}(t)]$. The coupled equations of motion are derived by following the procedure specified in Section 4. We obtain the following system of equations:

$$\ddot{a}_{mn} + \omega_{mn}^2 a_{mn} = -\Sigma_j\left[\ddot{p}_j + c_s^2\left(\frac{j\pi}{L_x}\right)^2 p_j\right]\alpha_{(mn)j}^{(p)}$$
$$-\Sigma_j\left[\ddot{q}_j + c_s^2\left(\frac{j\pi}{L_x}\right)^2 q_j\right]\alpha_{(mn)j}^{(q)} \qquad (62)$$

and

$$\ddot{p}_j + \omega_j^{cr2} p_j = -\frac{\rho c_A^2}{\sigma}\Sigma_{mn}\beta_{j(mn)}a_{mn}, \qquad (63)$$

$$\ddot{q}_j + \omega_j^{cr2} q_j = -\frac{\rho c_A^2}{\sigma}\Sigma_{mn}(-1)^{m+1}\beta_{j(mn)}a_{mn},$$

where

$$\alpha_{(mn)j}^{(p)} = \frac{\int\left[(1/2) + (y/L_y)\right]\xi_{mn}(x, y)\bar{\xi}_j(x)\,dx\,dy}{\int[\xi_{mn}(x, y)]^2\,dx\,dy},$$

$$\alpha_{(mn)j}^{(q)} = \frac{\int\left[(1/2) - (y/L_y)\right]\xi_{mn}(x, y)\bar{\xi}_j(x)\,dx\,dy}{\int[\xi_{mn}(x, y)]^2\,dx\,dy} \qquad (64)$$

and

$$\beta_{j(mn)} = \frac{\int\left[\partial\xi_{mn}(x, y)/\partial y\right]_{y=L_y/2}\bar{\xi}_j(x)\,dx}{\int[\bar{\xi}_j(x)]^2\,dx}. \qquad (65)$$

Thus we have obtained a system of linear second-order differential equations, which describes the time evolution of the square-box magnetar. These equations are solved by truncating all the series [i.e. restricting the range of indices (m, n, j)] and then by either solving the eigenvalue problem in order to find the normal modes, or by integrating the equations numerically.[10] One then checks that the series truncation does not introduce errors in the magnetar's motion within the frequency range of our interest.

So far we have worked in the approximation of the thin crust, i.e. we have effectively included the crustal modes which have no radial nodes in their wavefunction. However, several observed high-frequency QPOs, and in particular the strong QPO at 625 Hz (Watts

---

[10] Our favoured method here is again the energy-conserving second-order leapfrog. It is both fast and stable over long integration times.
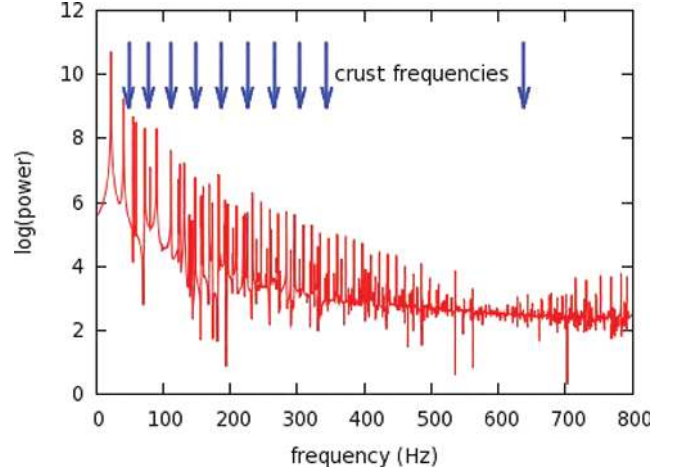

Figure 19. Power spectrum for the dynamics of a magnetized box as described in the text. In this particular model we have used the maximum possible shear modulus, corresponding to a maximally tangled field. The Alfvén motion in the box is coupled to nine of the lowest frequency 'crustal' modes, plus a high-frequency crust mode at 630 Hz.

& Strohmayer 2006) necessitate introduction of higher radial-order modes into our model. In the square-box model we do this phenomenologically, as follows. We assume that higher radial-order crustal modes have amplitudes $p_{sj}(t)$ and $q_{sj}(t)$ and natural eigenfrequencies ω_{sj}^{cr}, with s being the number of radial nodes, and assume that they cause displacement at the crust–core interface given by $\bar{\xi}_j(x)$. This mirrors realistic spherically symmetric case where the functional form of the crust–core displacement due to the torsional $\nabla \times Y_{lm}$ mode of the nth radial order is a very weak function n. The amplitudes $p_{sj}(t)$ and $q_{sj}(t)$ are then introduced on into the equations of motions (62) and (63) in the same way as the other p_j and q_j amplitudes, with the same j-dependent coupling coefficients but with ω_{sj}^{cr} instead of ω_j^{cr} on the left-hand side of equation (63).

We now have the basic ingredients of building a phenomenological modes with tangled fields. To sum up, we (1) quantify tangling using the effective shear modulus, (2) find discrete core eigenmodes and evaluate their coupling to the crustal model and (3) either find eigenfrequencies of the total star by diagonalizing the potential energy of the system, or simulate the time-dependent behaviour directly.

An example of a resulting power spectrum is shown in Fig. 19 for the model described in this section.

6 WHAT DO OUR MODELS TELL US ABOUT MAGNETAR QPOS?

In this paper we have developed a formalism which allows one to build a magnetar model with a variety of the spectral features of the core Alfvén waves, including continua with gaps and edges, and the large-scale discrete modes generated by the field tangling. We have constructed a number of magnetar models and explored the resulting QPOS, both for the case of axisymmetric magnetar with core Alfvén continuum, and for the 'square' magnetar models with the tangled fields (see the previous section). The full range of model parameters, and detailed comparison with the data will be the subject of a separate study. For now, we have restricted ourselves to the standard magnetar model, in which the core is a perfect conductor, the field of $\sim 10^{15}$ G penetrates both the core and the crust, and the proton fraction in the star is the one tabulated
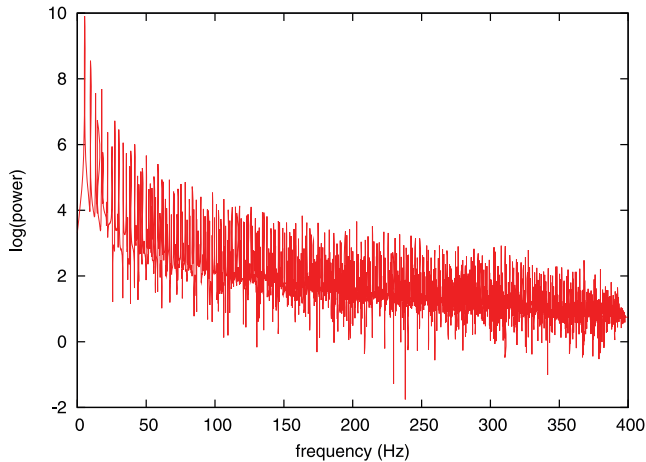
Figure 20. This spectrum was generated using a box model similar to the one from Fig. 19 but with neutron mass loading. Because of the mass loading the frequencies have shifted down by a factor of ~4. Note that there is no significant power above the lower edge-mode frequency of 5.3 Hz.

Figure 21. This spectrum was generated with the same box model as in Fig. 20, but in addition to the neutron mass loading, we have increased the magnetic field strength by a factor of 3. All frequencies above ~16 Hz are significantly damped.

in Haensel et al. (2007). Our models give us the following robust conclusions, as compared against QPO observations.

(1) A number of strong QPOs have been observed in the 1998 and 2004 giant flares, with frequencies ranging between 18 and 150 Hz (Israel et al. 2005, Strohmayer & Watts 2005; Watts & Strohmayer 2006). These QPOs can be qualitatively explained as gap and/or edge modes of Sections 4 and 2, or even transient QPOs of Section 3.[11] However, this was only possible if the neutrons were decoupled from the Alfvén waves in the core. If the neutrons took part in the Alfvén motion, then the effective mass of the Alfvén modes shifted up by a factor of 20–40 and their frequencies shifted down by a factor of 4–8 (Easson & Pethick 1979; Alpar, Langer & Sauls 1984; van Hoven & Levin 2008; Andersson, Glampedakis & Samuelsson 2009). As a result, all modes at frequencies above ~50 Hz were strongly damped (see Fig. 20). Increasing the magnetic field tension by a factor of 3 did not affect this conclusion (Fig. 21). For the spherical magnetar models of Section 4 we obtain similar results if couple the neutrons to the Alfvén motion in the core. The key point that we would like the reader to appreciate is that Alfvén modes in the core are key to determining the frequency and strength of the observable QPOs, and thus QPOs are very sensitive probe of the core interior.

(2) A number of the high-frequency QPOs have been measured in the 2004 giant flare by Watts & Strohmayer (2006), the strongest among them being the QPO at 625 Hz. This QPO is particularly strong and long-lived in the hard X-rays, reaching the amplitude of ~25 per cent over the time interval of ~100 s (i.e. it persists for almost 10^5 oscillation periods!). Watts & Strohmayer (2006) argued that this frequency corresponds to the crustal shear mode with a single radial node (see also Piro 2005); this interpretation, if correct, would strongly constrain the thickness of the crust and rule out the

fluid strange stars as magnetar candidates (Watts & Reddy 2007). To investigate this suggestion, we have introduced several high-frequency low-j crustal modes into our square-box simulations. However, as is demonstrated in Figs 14 and 15, the high-frequency modes are strongly damped and at no time during the simulations do we observe any significant power at those frequencies. This is to be expected. No natural axisymmetric model has gaps in the Alfvén continuum at such high frequencies, so global modes are strongly absorbed. We have argued that in realistic magnetic equilibria like the ones obtained by Braithwaite & Spruit (2004), field tangling will make continuum modes localized in small-scale flux tubes. Moreover, the field tangling creates a dense array of large-scale discrete modes, with the frequency separation between neighbouring modes being proportional to the degree of tangling. One could expect that if the Alfvén modes are discrete in the core due to field tangling, the absorption of high-frequency crustal modes would not arise. However, even in the discrete case the frequency spacing between the modes is around 20 Hz, which is much smaller than 600 Hz. Thus the grid of Alfvén waves is so dense that it is effectively seen as the absorbing continuum by the modes around 600 Hz. Our detailed simulations, of the type shown in Figs 14 and 15, fully confirm this qualitative picture.

The concern about the viability of high-frequency QPOs as being due to the physical oscillations of standard-model magnetars has been raised in the original L06 paper on the basis of rather simplistic calculations. As our work here shows, more detailed calculations partially alleviate the L06 concern for the frequencies below ~150 Hz, but only if the neutrons are decoupled from the Alfvén motion in the core, i.e. if at least one baryonic superfluid (protons or neutrons) is present in the neutron star core. Our analysis sustains L06 concern for the high-frequency QPOs, in particular for the strong long-lived QPO at 625 Hz. Its explanation seems to require either QPO production in the magnetosphere, or a somewhat radical revision of the magnetar model. Just how radical this revision has to be will be explored in a separate study.

Our work presented here has several shortcomings. We have limited ourselves to the linear approximation, and a non-linear regime may bring surprises. Direct non-linear simulations of axisymmetric oscillations of a magnetized fluid star have been carried out recently by Cerda-Duran et al. (2009). At this stage it is difficult to

---

[11] L07 and Gruzinov (2008b) associated the long-lived 18–20 Hz QPO with the lower edge of the Alfvén continuum. However, recent calculations of Steiner & Watts (2009) have argued that the crustal frequencies can be as low as 10 Hz due to the uncertainty in our theoretical knowledge of the crustal shear modulus. It is therefore plausible that the fundamental crustal mode has the proper frequency below that lower edge of the core Alfvén continuum. In this case, the 18–20 Hz QPO could be the gap mode which is dominated by the fundamental crustal mode.
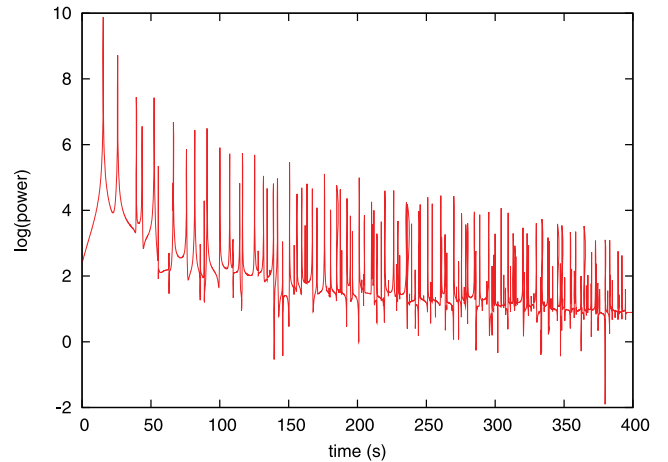
say whether non-linearities introduce significantly new QPO features to their model; their results have largely been in agreement with the linear simulations of Colaiuda et al. (2009). However, the computational techniques seem promising and we do not exclude that large-amplitude simulations of stars with the crust will show qualitatively new features. Another limitation of our work is that we have assumed that once the flare sets the magnetar into motion, the magnetar's oscillations are not driven externally. This may not be the case in real flares: some energy stored in the pre-flare magnetar may be released gradually, and this release could be extended in time into the flare's tail.[12] The latter consideration is straightforward to incorporate phenomenologically into our model, and we plan to address it in our future work.

ACKNOWLEDGMENTS

REFERENCES

Alladio F., Micozzi P., 1996, Phys. Plasmas, 3, 72
Alpar M. A., Langer S. A., Sauls J. A., 1984, ApJ, 282, 533
Andersson N., Glampedakis K., Samuelsson L., 2009, MNRAS, 396, 894
Barat C. et al., 1983, A&A, 126, 400
Braithwaite J., 2008, MNRAS, 386, 1947
Braithwaite J., Nordlund A., 2006, A&A, 450, 1077
Braithwaite J., Spruit H. C., 2004, Nat, 431, 819
Cerda Duran P., Stergioulas N., Font J., 2009, MNRAS, 397, 1607
Colaiuda A., Beyer H., Kokkotas K. D., 2009, MNRAS, 396, 1441
Douchin F., Haensel P., 2001, A&A, 380, 151
Duncan R. C., 1998, ApJ, 498, L45
Easson I., Pethick C. J., 1979, ApJ, 227, 995
Glampedakis K., Samuelsson L., Andersson N., 2006, MNRAS, 371, L74
Goedbloed J. P. H., Poedts S., 2004, Principles of Megnetohydrodynamics. Cambridge Univ. Press, Cambridge (GP)
Gruzinov A., 2008a, preprint (arXiv:0801.4032)
Gruzinov A., 2008b, preprint (arXiv:0812.1570)
Gruzinov A., 2009, preprint (arXiv:0905.0911)
Haensel P., Potekhin A. Y., 2004, A&A, 428, 191
Haensel P., Potekhin A. Y., Yakovlev D. G., 2007, Neutron Stars 1: Equation of State and Structure. Springer-Verlag, New York
Hollweg J. V., 1987, ApJ, 312, 880
Ionson J. A., 1978, ApJ, 226, 650
Israel G. L. et al., 2005, ApJ, 628, L53
Landau L. D., Lifshits E. M., 1976, Mechanics. Pergamon Press, Oxford, chap. V
Lee U., 2008, MNRAS, 385, 2069
Levin Y., 2006, MNRAS, 368, L35 (L06)
Levin Y., 2007, MNRAS, 377, 159 (L07)
Piro A., 2005, ApJ, 634, L153
Poedts S., Hermans D., Goossens M., 1985, A&A, 151, 16 (P85)
Samuelsson L., Andersson N., 2007, MNRAS, 374, 256
Sotani H., Kokkotas K. D., Stergioulas N., 2008, MNRAS, 385, L5
Steiner W., Watts A. L., 2009, Phys. Rev. Lett., 103, 1101
Strohmayer T. E., Watts A. L., 2005, ApJ, 632, L111
van Hoven M., Levin Y., 2008, MNRAS, 391, 283
Watts A. L., Reddy S., 2007, MNRAS, 379, L63
Watts A. L., Strohmayer T. E., 2006, ApJ, 637, L117

---

[12] We thank Chris Thompson for pointing out this possibility.

APPENDIX A: MULTIMODAL CRUST–CORE SYSTEM

In this appendix we generalize the normal-mode treatment of Section 2.2, and write down the general prescription of how to find the eigenmodes when *several* 'large' crustal shear modes are coupled to a multitude of small core Alfvén modes, provided the coupling coefficients are known. In this paper, the coupling coefficients are worked out in simple models of Sections 4 and 5; we shall postpone the discussion of how the coefficients are computed in more general case to the future paper.

Let us denote the displacement of the crustal and core modes by X_n and x_i, respectively. Since both the crustal and the core modes are not directly coupled to themselves (i.e. Xs are only coupled to xs), most general equations of motion take the form

$$\ddot{X}_n + \Omega^2 X_n = \Sigma_i \alpha_{ni} x_i,$$
$$\ddot{x}_j + \omega_j^2 x_i = \Sigma_m \beta_{jm} X_m, \tag{A1}$$

where Ω_n and ω_j are the proper frequencies of the crustal and core modes, and αs and βs are the coupling coefficients. We look for an oscillatory solutions of the above equations with angular frequency Ω. One can trivially rewrite these equation as a matrix eigenequation with Ω^2 as an eigenvalue, and solve it using standard methods. However, if the number of crustal modes is not too large, it is convenient to make a shortcut. Using the second of equation (A1) to express x_is through X_ns, and substituting into the first one, we get the following equation:

$$\Sigma_n G_{mn}(\Omega) X_n = 0, \tag{A2}$$

where the elements of the matrix G are given by

$$G_{mn}(\Omega) = (\Omega^2 - \Omega_n^2)\delta_{nm} + \Sigma_i \frac{\alpha_{ni}\beta_{im}}{\omega_i^2 - \Omega^2}. \tag{A3}$$

One obtains the eigenfrequencies by finding numerically the zeros of det G_{mn}.

APPENDIX B: CORE CONTINUA WITH A MIXED AXISYMMETRIC TOROIDAL–POLOIDAL MAGNETIC FIELD

In this appendix we will calculate the continuum of Alfvén frequencies in a magnetar core in the case of a axisymmetric magnetic field with mixed toroidal and poloidal components. The general MHD equations of motion for spherically symmetric, self-gravitating equilibrium with an axisymmetric field are derived in detail in P85. In contrast to the special case of a purely poloidal field (see Section 4.2) which leads to two uncoupled differential equations, the continuum for a mixed toroidal–poloidal field is described by a system of fourth-order coupled ODEs. Because of this coupling, the solutions are complicated as they are no longer polarized in the directions parallel (so-called 'cusp solutions') and perpendicular (Alfvén solutions) to the magnetic field lines, but rather have a mixed character. Strictly speaking, one can only speak of an 'Alfvén continuum' in the limit that the variations in ρ, P and B^2 are small in the magnetic flux surfaces. The general equations of motion are given in equations (53) and (54) of P85. We note, however, that in magnetars the speed of sound $c \gg c_A$, and therefore we consider P85's equations (53) and (54) in the incompressible limit (P85,

equations 73 and 74). For completeness we give the equations here,

$$\rho\sigma^2 \frac{B_\chi^2 B^2}{B_\phi^2} Y = B^2 F \frac{B_\chi^2}{B_\phi^2 B^2} F\left(\rho c_A^2 Y\right) + \frac{1}{\rho c_A^2}\left[\frac{\partial}{\partial\chi}\left(\rho c_A^2\right)\right]^2 Y$$

$$+ \rho B_\chi^2 N_\chi^2 (Y+Z) - \frac{\partial}{\partial\chi}\left(\rho c_A^2\right) FZ, \qquad \text{(B1)}$$

$$\rho\sigma^2 B^2 Z = i F\left[\frac{\partial}{\partial\chi}\left(\rho c_A^2\right) Y\right] + \rho B_\chi^2 N_\chi^2 (Y+Z) + F\left(\rho c_A^2 FZ\right). \qquad \text{(B2)}$$

The variables $Y \equiv i\left(B_\phi^2 \xi_\chi - B_\phi B_\chi \xi_\phi\right)/B_\chi B^2$ and $Z \equiv i(B_\chi \xi_\chi + B_\phi \xi_\phi)/B^2$ are components of the fluid displacement perpendicular and parallel to the magnetic field lines, the operator $F \equiv i\partial/\partial\chi$ is a differential operator along the field lines, $N_\chi \equiv -\left(1/B_\chi\rho\right)\sqrt{(\partial\rho/\partial\chi)(\partial P/\partial\chi)}$ can be thought of as a Brunt–Väisälä frequency for displacements along the field lines. According to Gauss' law for magnetism, the toroidal component of the magnetic field is of the form $B_\phi = f(\psi)/\varpi$, where ϖ is the distance to the polar axis, and $f(\psi)$ is an arbitrary function of ψ. In the following calculation we adopt a toroidal field component of the form

$$B_\phi = \frac{B_{t,0} R_*}{\varpi(\chi)} \sin\left(\theta(\psi)\right). \qquad \text{(B3)}$$

Here $\theta(\psi)$ is the polar angle at which the flux surface ψ intersects the stellar crust. Clearly this choice for B_ϕ is completely arbitrary and one could in principle try many different toroidal geometries.

As with our calculation of the Alfvén continuum in the case of a purely poloidal field (Section 4.2), we adopt the zero-displacement boundary conditions at the crust, and use the fact that our equilibrium model is (point-) symmetric with respect to the equatorial plane. This enforces the existence of classes of symmetric and antisymmetric eigenfunctions, $Y_n(\chi)$ and $Z_n(\chi)$. We consider only the odd modes, and calculate the eigenfunctions by means of the shoot-
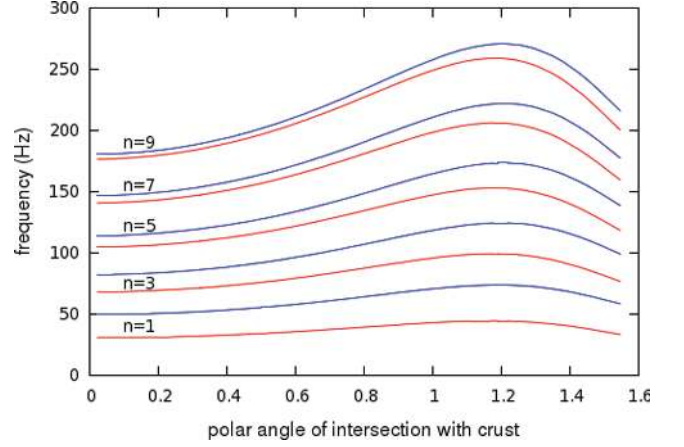

Figure B1. The curves show the continuum frequencies σ_n as a function of the angle $\theta(\psi)$, the polar angle at which the flux surface ψ intersects the crust. In the presence of a toroidal field, the degeneracy between the cusp solutions and the Alfvén solutions is broken and we find two separate solutions for each wavenumber n; waves with primarily Alfvén character (red curves) and waves with primarily cusp character (blue curves). This particular continuum was calculated using a poloidal field with an average surface value $B_{p,surface} \sim 6 \times 10^{14}$ G (again generated by a circular ring current of radius $a = R_*/2$) and a toroidal field strength at the equator and the crust–core interface of $B_{t,0} = 3 \times 10^{14}$ G (see equation B3).

ing method; we use a fourth-order Runge–Kutta scheme to integrate equations (B1) and (B2). Starting with $Y(0) = 0$ and $Z(0) = 0$ at the equator, we integrate outward until we reach the crust at $\chi = \chi_c$. We find the eigenfrequencies by changing the value of σ until we match the boundary conditions at the crust. A resulting continuum is plotted in Fig. B1.

This paper has been typeset from a TEX/LATEX file prepared by the author.